Journal of
Materials Chemistry A

ROYAL SOCIETY
OF CHEMISTRY

PAPER

View Article Online
View Journal | View Issue

Check for updates

Cite this: *J. Mater. Chem. A*, 2024, **12**, 2465

The role of oxygen in automotive grade lithium-ion battery cathodes: an atomistic survey of ageing†

Anastasiia Mikheenkova,[a] Soham Mukherjee,[b] Moritz Hirsbrunner,[b] Pontus Törnblom,[b] Cheuk-Wai Tai,[c] Carlo U. Segre,[d] Yujia Ding,[d] Wenliang Zhang,[e] Teguh Citra Asmara,[e] Yuan Wei,[e] Thorsten Schmitt,[e] Håkan Rensmo,[b] Laurent Duda[b] and Maria Hahlin*[ab]

The rising demand for high-performance lithium-ion batteries, pivotal to electric transportation, hinges on key materials like the Ni-rich layered oxide $LiNi_xCo_yAl_zO_2$ (NCA) used in cathodes. The present study investigates the redox mechanisms, with particular focus on the role of oxygen in commercial NCA electrodes, both fresh and aged under various conditions (aged cells have performed >900 cycles until a cathode capacity retention of ~80%). Our findings reveal that oxygen participates in charge compensation during NCA delithiation, both through changes in transition metal (TM)–O bond hybridization and formation of partially reversible O_2, the latter occurs already below 3.8 V *vs.* Li/Li^+. Aged NCA material undergoes more significant changes in TM–O bond hybridization when cycling above 50% SoC, while reversible O_2 formation is maintained. Nickel is found to be redox active throughout the entire delithiation and shows a more classical oxidation state change during cycling with smaller changes in the Ni–O hybridization. By contrast, Co redox activity relies on a stronger change in Co–O hybridization, with only smaller Co oxidation state changes. The Ni–O bond displays an almost twice as large change in its bond length on cycling as the Co–O bond. The $Ni–O_6$ octahedra are similar in size to the $Co–O_6$ octahedra in the delithiated state, but are larger in the lithiated state, a size difference that increases with battery ageing. These contrasting redox activities are reflected directly in structural changes. The NCA material exhibits the formation of nanopores upon ageing, and a possible connection to oxygen redox activity is discussed. The difference in interaction of Ni and Co with oxygen provides a key understanding of the mechanism and the electrochemical instability of Ni-rich layered transition metal oxide electrodes. Our research specifically highlights the significance of the role of oxygen in the electrochemical performance of electric-vehicle-grade NCA electrodes, offering important insights for the creation of next-generation long-lived lithium-ion batteries.

Received 11th September 2023
Accepted 6th December 2023

DOI: 10.1039/d3ta05516g

rsc.li/materials-a

1 Introduction

The strong need for transport electrification as a global warming mediation tool drives battery research towards more sustainable solutions.[1] Layered oxide Ni-rich electrodes (Ni > 60%) are rapidly gaining in the electromobility market, favoured due to their relatively high capacity and high energy density.[2] At the same time, the advantages come at a cost of lower safety and material stability.[3] With a higher nickel content, these materials operate at potentials which are associated with structural deterioration, oxygen evolution and electrolyte oxidation, processes that need to be mitigated for providing long-term stable batteries.[4] The investigation and understanding of the deterioration trends are however challenging as they are dependent not only on the chemistry of the material[5] (*e.g.*, Ni content in Ni-rich layered oxides such as $LiNi_xMn_yCo_zO_2$ (NMC) and $LiNi_xCo_yAl_zO_2$ (NCA),[6] type of doping,[7,8] and the composition gradient[9]), but also on cycling conditions such as the State of Charge (SoC) window, temperature, pressure, cycling rate, *etc.*[10–12]

Using Ni-rich NCA electrodes extracted from electric car battery pack cells, our group has shown that the positive electrode performance is both sensitive towards cycling beyond 50% state of charge (~3.8 V) and that degradation is enhanced

---

[a] *Ångström Laboratory, Department of Chemistry, Uppsala University, SE 751 21 Uppsala, Sweden. E-mail: maria.hahlin@kemi.uu.se*

[b] *Ångström Laboratory, Department of Physics and Astronomy, Uppsala University, SE 751 21 Uppsala, Sweden*

[c] *Department of Materials and Environmental Chemistry, Arrhenius Laboratory, Stockholm University, Stockholm, 10691, Sweden*

[d] *Department of Physics and CSRRI, Illinois Institute of Technology, Chicago, IL 60616, USA*

[e] *Laboratory for Condensed Matter, Paul Scherrer Institute, Forschungsstrasse 111, Villigen PSI, 5232, Switzerland*

† Electronic supplementary information (ESI) available. See DOI: https://doi.org/10.1039/d3ta05516g

when the battery is cycled at elevated temperature (45 °C).[12] Loss of active material (LAM) in the cathode is a common occurrence for all studied conditions (0–50, 50–100, and 0–100% SoC ranges and at room and elevated temperatures). Transition metal dissolution and cation mixing together with a simultaneous increase in the lithium-ion diffusion resistance coefficient can partially explain the decreased performance of the aged electrodes. Perhaps, most importantly, a previous study[12] shows that the established degradation mechanisms such as particle cracking and phase transformation cannot fully explain the observed LAM in these highly engineered cathode materials, thus inviting deeper insights in order to establish more effective mitigation strategies to tackle the performance deterioration. In this context, the current study uses the same electrodes as studied in ref. 12 and 13 to investigate the role of oxygen in electrochemical performance and ageing in Ni-rich transition metal oxide materials.

Among the degradation mechanisms that are common for Ni-rich electrodes, gas evolution, of oxygen in particular, has generated tremendous interest in the battery research community, as it has substantial consequences on battery safety and performance.[14,15] The oxygen in the evolved gas mixture has been found to originate from the cathode material.[16] Oxygen evolution from NCA-type cathode materials is often attributed to the electrochemical decomposition of lithium carbonate from the surface of the particles[17] and/or from oxygen evolving from the structure as a result of charge compensation during battery cycling.[18] A previous study by our group demonstrates that gas evolution together with lithium-ion diffusion resistance coefficient increase correlates with bulk structural changes.[13] For Ni-rich electrodes, both mechanisms are triggered at higher potentials and typically observed at potentials above 4.2 V *vs.* Li/Li^+.[13,15,16]

The simplified model of lithium-ion battery (LIB) operation accounts only for cationic redox, where the charge compensation during cathode delithiation comes from the transition metals. However, it has been shown that Ni-rich oxides tend to evolve oxygen beyond 75% delithiation (~4.2 V *vs.* Li/Li^+).[19–21] It is suggested that the delithiation of Ni-rich cathodes affects the covalency of the transition metal (TM)–O bond and that a partial transfer of negative charge from oxygen to nickel occurs in order to compensate for the charge, which is followed by oxygen leaving the lattice. In the battery community, this process is commonly referred to as "oxygen redox" or "anionic redox". However, the full role of oxygen in the electrochemical activity of Ni-rich materials is yet not fully understood. Recently it was proposed that the covalency degree of the transition metal–oxygen bonds within the material will limit the average discharge potential rather than just the availability of Ni^{2+}.[18] The influence of oxygen-related processes on battery performance, however, goes beyond this effect. It has been shown that the distance between Li–O slabs in the layered structure serves as an energy barrier for lithium intercalation and deintercalation, thus adding resistance during cell cycling.[13,22] Additionally, it is proposed that oxygen release enhances particle cracking.[23] These processes are all connected to battery performance and are seen to link to LIB degradation upon long-term use.[24] This highlights the importance of oxygen-related degradation studies and particularly the evaluation of the extent of the oxygen-related reversible and irreversible processes occurring during battery cycling.

The process of cathode degradation associated with oxygen release has been studied with various methods. One of the most common ways is to measure CO_2 and CO reaction products in the gas that evolve from a cell.[16,25] However, this method is indirect and considers only oxygen that is released from the surface of the electrode which either originated at the interface between the cathode active material and electrolyte or migrated to the surface of the particle and subsequently reacting with the electrolyte.[26] A great advancement in exploring oxygen redox activity in the bulk was made using Resonant Inelastic X-ray Spectroscopy (RIXS) for Li-rich layered oxide electrodes.[27,28] The possibility to observe oxygen redox and follow the formation of molecular oxygen within the bulk of the active material has opened new prospects for in-depth investigation of the oxygen-driven degradation mechanism also in Ni-rich materials. Furthermore, the oxidation states and local environment of the surrounding transition metal can be followed using X-ray absorption spectroscopy (XAS) and Extended X-ray Absorption Fine Structure Spectroscopy (EXAFS) particularly.[29] Such results have indicated a decrease of the electrochemical activity of Ni and Co after the cell had operated for 100 cycles.[29] For these types of materials, various examples of observed oxygen-related degradation processes were also studied using Transmission Electron Microscopy (TEM), which is particularly effective in determining the crystal structure in the surface of the layered lithium transition metal oxide particles.[30]

In the current study, we combine RIXS, XAS/EXAFS and TEM results to access the redox activity linked to individual TM ions and oxygen and the change in its reversibility after ageing in automotive grade NCA-based electrodes extracted from cells operated in a commercial battery pack. The choice of the material is motivated by its high quality and its commercial availability as well as targeting the gap in industrial and academic battery material research. Here we address a difference in the electrochemical activity of $Ni–O_6$ and $Co–O_6$ octahedral environments upon ageing as well as considering oxygen participation observed with RIXS and XAS: through hybridization of TM–O bonds and oxygen redox. Highlighting the main results of the study, firstly, the contraction and expansion of TM-oxide octahedra upon cycling are larger for Ni compared to Co and that $Ni–O_6$ volume is enhanced upon ageing. Secondly, the formation of molecular O_2 is a fundamental oxygen redox process in this Ni-rich NCA material being visible below 3.8 V *vs.* Li/Li^+ and still visible after ~900 cycles. Thirdly, the ageing is associated with the formation of a large number of nanosized voids in the bulk of the NCA particles. A more comprehensive discussion section puts the combined XAS, RIXS, and TEM results in the context of ageing mechanisms generally discussed in the literature.

2 Results

The scheme of the sample preparation and naming of the samples in this article together with their relation to a previous study[12] is shown in Fig. 1. The samples studied in the current work were either used as extracted from a fresh electric car battery pack (sample Fresh) or extracted after the electrodes were aged in a full cell either within a 0–50% (sample Aged L) or 0–100% (sample Aged H) SoC window until the battery reached 75% of initial capacity (see details in the ESI "Cell tear-down"†). In order to observe changes at different states of charge, samples of each set of ageing conditions were assembled into pouch cells and brought to different lithiation states and the samples are here further expressed in terms of SoC: 0%, 50% and 100% SoC correspond to extraction from the pouch cells at 2.55 V, 3.8 V, and 4.2 V *vs.* Li/Li$^+$ respectively. The electrochemical curves are presented in Fig. S2 in the ESI "Sample preparation" section.† These samples are named Fresh 0/Aged L 0/Aged H 0, Fresh 50/Aged L 50/Aged H 50, and Fresh 100/Aged L 100/Aged H 100 correspondingly, where the last number indicates the SoC of the material (ESI "Experimental" section†). The samples were studied using hard and soft X-ray XAS, RIXS and TEM and the details of the experiments can be found in the ESI "Experimental", "TEM", "EXAFS analyses", and "RIXS" sections.† The soft X-ray XAS and RIXS investigations were performed at the ADRESS beamline of the Swiss Light Source at the Paul Scherrer Institut. Below the results are organized based on the specific phenomenon being examined. Initially, we show the morphological changes in the NCA material upon ageing. Then, we employ both hard and soft X-rays to examine the element specific redox activity of Ni and Co, which are generally recognized as the primary redox centers, but which are strongly linked to the activity of oxygen in this NCA material ($LiNi_{0.90}Co_{0.05}Al_{0.05}O_2$). Finally, we use XAS and RIXS to directly target the oxygen redox activity. As stated in the Introduction, these cathodes were previously investigated in a general ageing study, and for a more comprehensive electrochemical evaluation of the cathodes introduced above we refer the reader to that article.[12]

2.1 Morphology of the primary NCA particles

Particle cracking and morphological changes are often suggested as a LAM mechanism of cathode degradation. To study such changes for the aged NCA particles, both SEM and TEM measurements were done. The SEM images show that the active material in the NCA cathodes consists of spherical polycrystals ∼10 μm diameter composed of ∼100 nm sized crystallites (SEM image of the particle is presented in the ESI "SEM" section†). Fig. 2 presents high-angle angular dark-field scanning transmission electron microscopy (HAADF-STEM) images of the Fresh (a) and Aged H 0 (b, c, and d) electrodes. The areas of interest were taken for similar positions of the primary particles within the secondary particles (Fig. S3† shows the SEM image showing primary and secondary particles). The particles contrast in light grey on the images. Slight cracks are observed for both Fresh and Aged H electrodes, and a significant increase in cracking after ageing cannot be observed. Still, a substantial visual change in the electrode morphology is present. Dark regions in the range of a couple to a hundred nanometers, related to void (nanopores) formation, are visible inside the particles of Aged H samples.

Upon detailed observation of the primary particles in Aged H electrodes, one can notice that some of the voids are concentrated along the edges of the particles, while none of them seems to be migrating through the surface (Fig. 2c and d). Some of the voids are more significant in size. However, in the pore size distribution analysis (Fig. 2e) it can be seen that most of the pores are in size between 4 and 8 nm. The TEM analysis was conducted in 3 regions; however, due to the statistical limitations it is possible that the sampling volume does not represent the whole electrode. Nevertheless, all of the obtained TEM images showed the same morphology. The TEM images do not provide direct information on how the pore formation relates to oxygen activity, but based on the results presented below, one hypothesis is a link to irreversible O_2 release that propagates through the lattice and appears closer to the NCA surface. The RIXS results below suggest that these voids are not permanently filled with O_2 gas. The topic of pore formation will be further considered in the Discussion section.

2.2 Ni and Co charge compensation mechanisms and their change with ageing

Hard X-ray XAS is an element-specific technique widely used for the identification of the chemical state and local environment

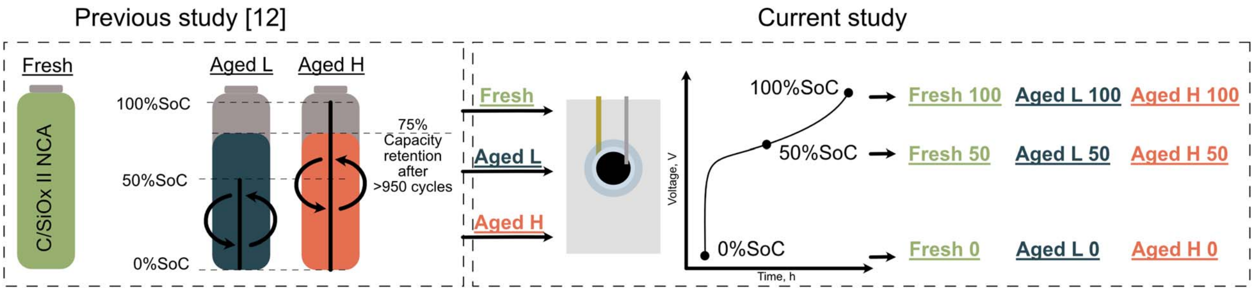

Fig. 1 In the current study, the NCA positive electrodes Fresh, Aged L and Aged H extracted from cells were also investigated in a previous study with a focus on ageing mechanisms automotive cells.[12] Aged electrodes are extracted from cells that performed >900 full cycle equivalents and the capacity retention of the positive electrodes was ∼75%. The difference in the two ageing cases is that one cell was continuously cycled between 0 and 50% SoC (in this article referred to as Aged L) and another between 0 and 100% SoC (Aged H). The extracted electrodes were reassembled in pouch half-cells and delithiated to 50% SoC and 100% SoC. The naming of the samples reflects the state of the sample (Fresh, Aged L or Aged H) and state of charge (0, 50, or 100% SoC).

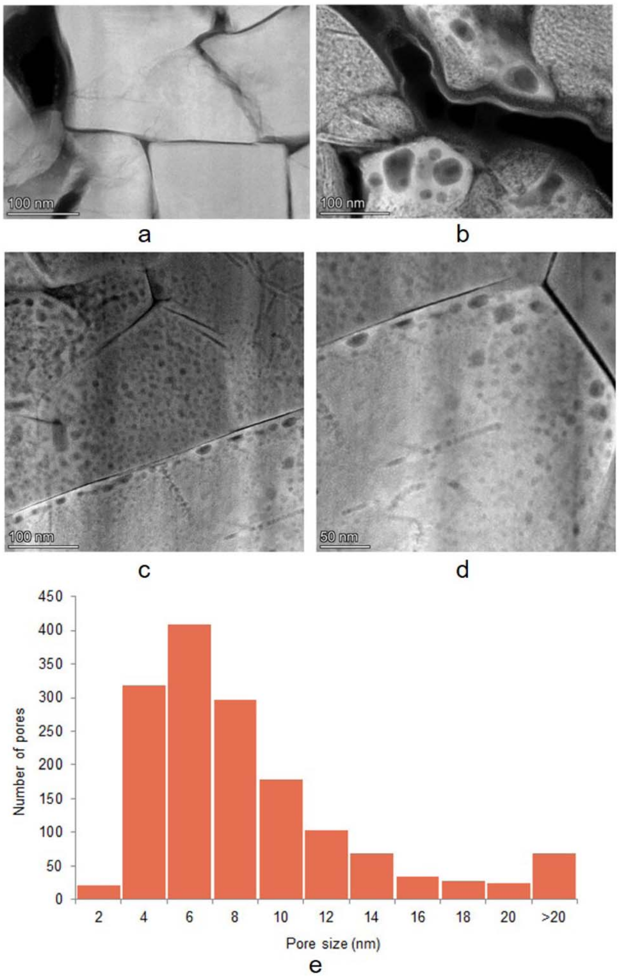

Fig. 2 HAADF images of the Fresh 0 and Aged H 0 samples and pore distribution histogram: (a) HAADF images of Fresh 0 NCA primary particles within the electrode; (b–d) HAADF images of Aged H primary particles within the electrode. The pore size distribution histogram derived from the Aged H 0 image analysis (e).

of transition metals, with the sampling depth that discloses primarily bulk information. Fig. 3 shows the X-ray absorption near edge (XANES) spectra for (a) Ni K- and (b) Co K-edges for NCA electrodes in the fresh state and after the samples underwent different ageing conditions (Fresh, Aged L and Aged H), alongside the Ni and Co metal foils. The estimated absorption energy positions for Fresh 0 (E_{A1}) and Fresh 100 (E_{A2}) are marked in both figures and demonstrate the difference in Ni and Co oxidation states upon material delithiation. One can immediately notice a much larger chemical shift ($\Delta E = E_{A2} - E_{A1} \sim 2$ eV) for Ni as compared to the Co edge ($\Delta E \sim 0.7$ eV) when going from 0% SoC to 100% SoC for the fresh electrode, and all the aged electrodes exhibit similar behaviour. Still, the absorption profile for the Ni K-edge differs significantly between fresh and aged samples, as compared to the more similar Co K-edges. This clearly indicates considerable changes in the local environment around Ni on ageing, while only minor changes occur in the local environment around Co. The white line intensities (a term that refers to the rising absorption edge), related to electronic transitions from 1s → unoccupied 4p states, correlate to the population of unoccupied TM 4p states at the conduction band edge. The ageing is seen to decrease the white line intensity, showing the decrease in the number of unoccupied Ni 4p states. As expected, the white line feature shifts to higher energies on delithiation, but for both ageing conditions it also broadens. While ageing can be determined to primarily involve changes around the Ni environment, the origin of the changes in the white line character is hard to determine. The complexity of the structure can result in artefacts in the spectrum coming from interactions with surrounding elements. In order to fully resolve it, aid from advanced theoretical modelling is required.

Feature B, marked for both K-edges in Fig. 3, correlates to transitions to the d-states of neighbouring metal (M) sites, *i.e.*, oxygen-mediated intersite M(4p)–O(2p)–M(3d) hybridization.[31,32] Feature B is evident for Co K-edges at 0% SoC, but becomes negligible at 100% SoC, in the case of both the fresh and aged electrodes. For Co, a higher state of charge, *i.e.* cathode delithiation, is thus seen to reduce the extent of intersite hybridization and the bond character shifts from covalent to more ionic. For Ni, feature B is not evident in the fresh sample at 0% SoC, showing only minor intensity. At 0% SoC, the degree of covalency of the Ni–O bond in the fresh electrodes is thus lower than for the Co–O bond. However, for Ni feature B increases for the aged samples (0% SoC), but yet not reaching the same intensity change as seen for Co. This implies that ageing increases the level of M(4p)–O(2p)–M(3d) hybridization for Ni. In Aged H 100 and Aged L 100 electrodes, feature B diminishes for Ni, similar to Co. Thus, ageing is seen to change the Ni environment to allow a reversible change from covalent towards ionic bond character upon lithiation and delithiation, while for Co the extent of hybridization change is similar for Fresh and Aged electrodes. A combination of all the XANES results suggests that during delithiation of the Fresh cathodes, it is Ni which is the main source of the charge compensation in the Ni–O_6 octahedron, while changes in the hybridization of the Co–O bond with less participation of Co takes place in the Co–O_6 octahedron. In terms of the charge compensation mechanism, Ni becomes more similar to Co after ageing, and their initial difference may link to the lower stability of the Ni-rich layered oxide cathodes.

Also, direct Ni p–d mixing increases with ageing. This is seen from the enhancement of feature C of the pre-edge structure (insets of Fig. 3). Feature C is related to quadrupolar transitions: M 1s → 3d (t_{2g}) and 3d (e_g) caused by symmetry breaking around the metal sites which allows p–d mixing.[33,34] For Ni, feature C is clearly higher in the aged delithiated samples, while for Co all samples show a similar peak intensity, and this supports higher changes occurring with Ni on ageing. We further notice a larger shift of the peak positions to higher energies at delithiation for Ni compared to Co, which is in correspondence with the shift of the main absorption energy positions. The pre-edge peaks corresponding to Ni are typically broader than for Co, suggesting higher disorder around Ni sites. On delithiation, feature C is generally narrower and gains intensity, showing an increased ordering. This is most evident

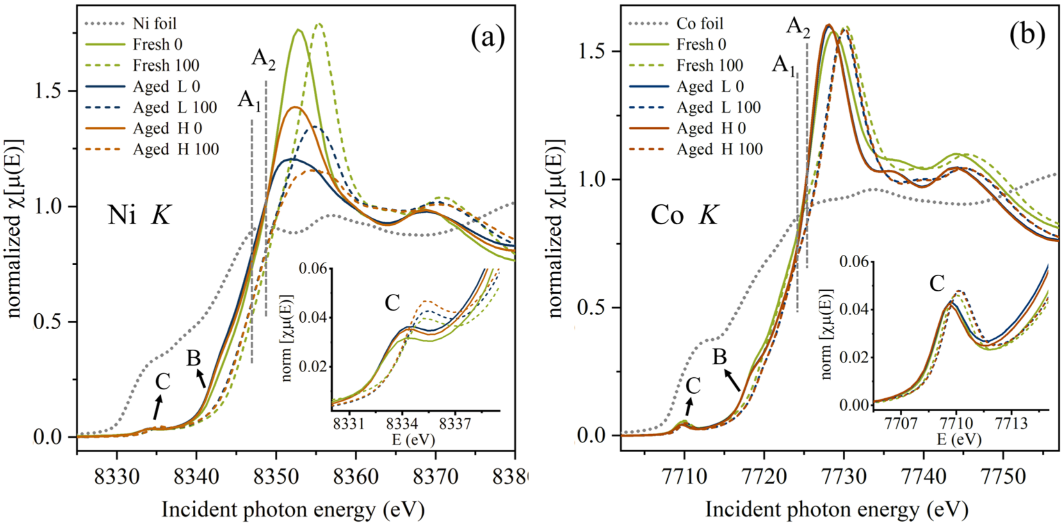

Fig. 3 Comparative XANES data for (a) Ni K- and (b) Co K-edges for Fresh (green) and aged NCA electrodes (Aged L in blue; Aged H in orange); solid and dotted traces indicate 0% SoC and 100% SoC, respectively, including Ni and Co metal references. Corresponding insets show a magnified view of the pre-edge fine structures for Ni K- and Co K-XANES.

for Ni, and a similar trend is seen irrespective of ageing conditions. Together the changes in features B and C show that upon delithiation both TM–O_6 environments undergo local structural modifications related to increased ordering around either oxygen or TM sites, or both. These changes are more distinct for Ni, most likely due to stronger oxidation effects compared to Co in the NCA electrodes during delithiation.

The larger changes in the Ni–O_6 environment warrants an extended evaluation of also Ni L-edge XAS. This allows complementary understanding of changes in Ni oxidation states, as well as the associated t_{2g} and e_g symmetry states. The transition metal L-edge XAS data indicate that nickel changes from a lower to a higher oxidation state on delithiation, supporting the finding from the Hard X-ray study of the Ni K-edge shown above. Fig. 4 displays Ni L-edge XAS spectra collected in total fluorescence yield (TFY) modes (PFY XAS spectra can be found in ESI Fig. S11†). Here, both the Ni L-edge TFY modes display an intensity shift from the lower to the higher energy peak, albeit minor for the PFY, in the L_3-area during delithiation, signaling an increased oxidation state.

The investigation of both the L_3- and L_2-peaks reveals that during delithiation there is a broadening to the high energy side of the peaks, while the low energy side remains at the same incident energy for all samples. The broadening of the high energy side indicates that some nickel is oxidizing towards a higher oxidation state, while the unchanged position of the low energy side indicates that some nickel remains in the lower oxidation states. This suggests that the oxidation change in the NCA is not uniform, with some nickel remaining in its lower oxidation states while other nickel changes towards even higher oxidation states on delithiation.

Finally, comparing the Ni L-edge TFY spectral shapes from the Aged 0, 50, and 100% SoC, seen in Fig. S7 in the ESI,† their character is slightly different between the 0, 50, and 100% SoC with a greater difference between Fresh and both aged at 50% SoC. This suggests that nickel's electronic structure changes during ageing with the most significant changes when aged between 0 and 50% SoC. The difference between all samples is present at 100% SoC with Aged H demonstrating higher discrepancy among all samples.

2.3 Local atomic structure around the transition metals

Revisiting the TM K-edges, the local atomic structure around the TM can be understood from their EXAFS regions. The $\chi(k)$

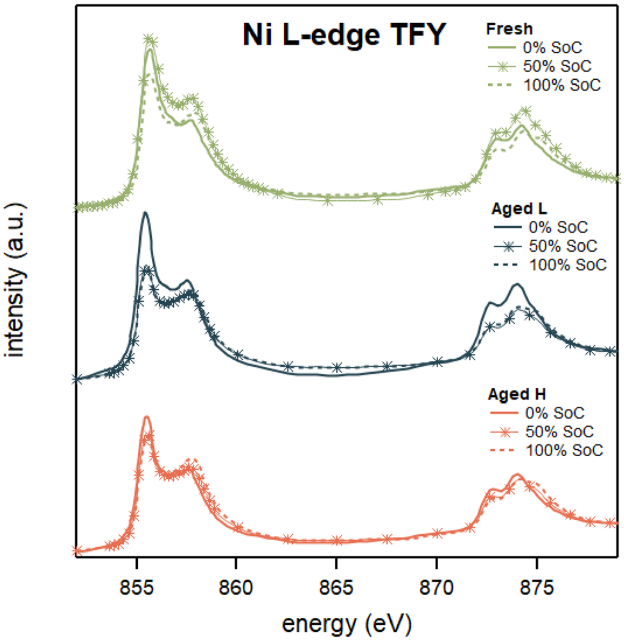

Fig. 4 Ni L-edge XAS spectra collected in the TFY of Fresh 0, Fresh 50, Fresh 100, Aged L 0, Aged L 50, Aged L 100, Aged H 0, Aged H 50, and Aged H 100.

functions were Fourier transformed using k^2-weighing (details are specified in the ESI "Hard XAS/EXAFS", "EXAFS analyses" and "EXAFS" sections†); the modulus of the Fourier transform (mod[$\chi(R)$]), hereafter referred to as $\chi(R)$, is shown in Fig. 5. Correlating the positions of different peaks in the $\chi(R)$ data to crystallographic information of hexagonal symmetry in NCA materials, we can assign different coordination shells within the Ni/Co local structure (Fig. 5g). Here peak D (first shell) in $\chi(R)$ corresponds to the nearest O neighbours. Peak E (second shell) in $\chi(R)$ corresponds to combined scattering from the next metal sites (Co, Ni and Al), both intralayer (in χab plane) and interlayer (along χc axis), as well as Li ions in between the TM–O layers. Peak F is related to the shell that contains transition metals and Al. The $\chi(R)$ amplitude for region F is dominated by the number of Ni/Co ions, and to a lower extent by Al. Li contribution is rather insignificant with no perceivable changes upon delithiation. The next two regions G and H correspond to the positions of the second next neighbouring metal sites (Al, Co, Ni and Li) occurring along all three lattice directions. In Fig. 5, we show the $\chi(R)$ functions of Ni and Co respectively for fresh electrodes (a and b), for aged L (c and d), and aged H (e and f) under lithiated and delithiated conditions.

A comparison of the $\chi(R)$ features for Ni and Co ($\chi(R)^{\mathrm{Ni}}$; $\chi(R)^{\mathrm{Co}}$) in Fig. 5 reveals several contrasting changes between the two metal sites. Firstly, we find the overall intensity variations of peaks D and E with delithiation to be rather different in $\chi(R)^{\mathrm{Ni}}$

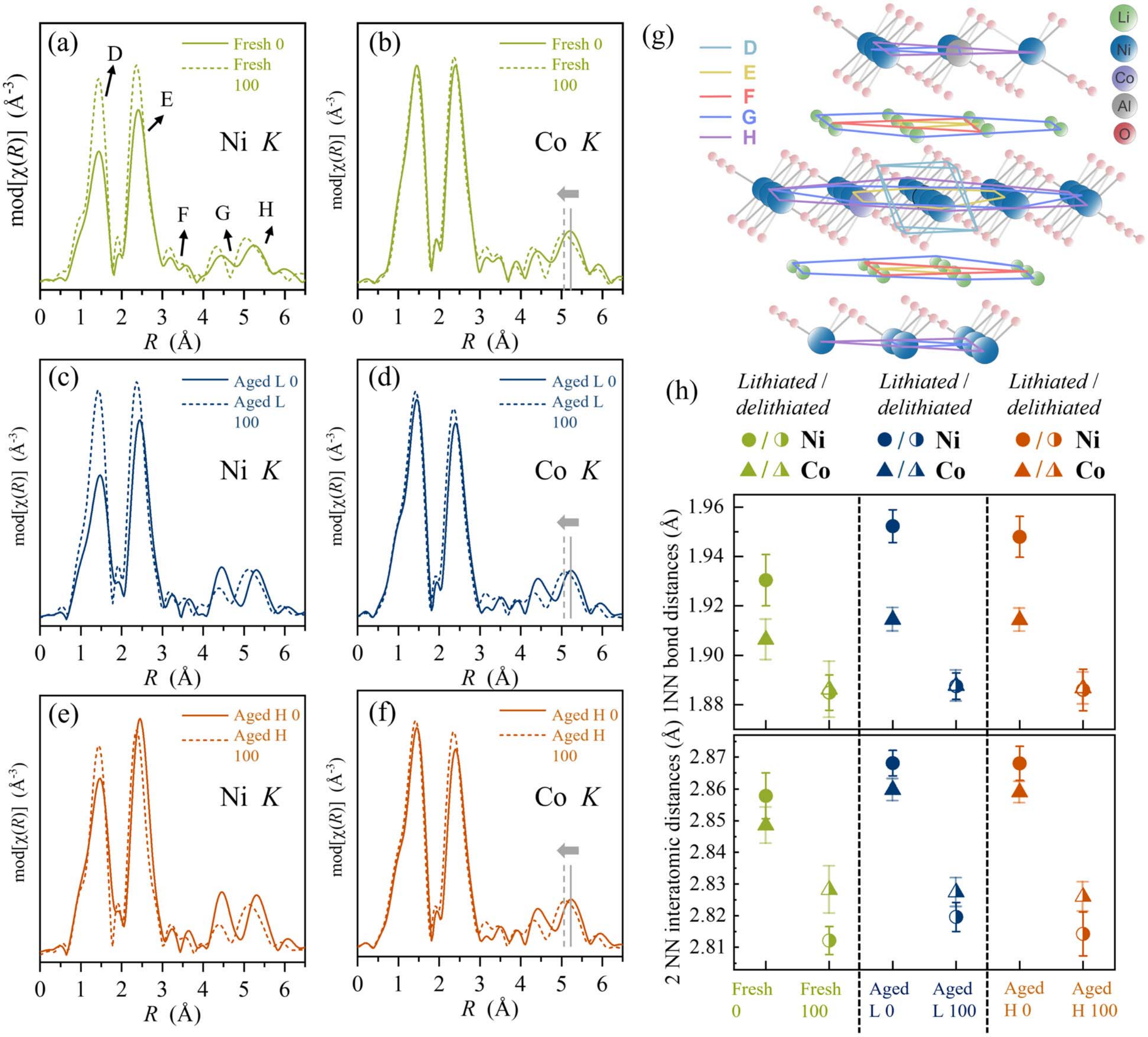

Fig. 5 Modulus of Fourier transformed χ(R) data for Ni (left column) and Co (right column) K-edges for (a and b) Fresh (c and d) Aged L and (e and f) Aged H electrodes at 0% SoC (solid lines: lithiated) and 100% SoC (dotted lines: delithiated), revealing stronger changes in Ni EXAFS compared to Co, as well as a clear shrinking of the local environment, indicated by vertical markers (grey lines). The NCA supercell with several examples of shells is demonstrated (g). Comparison of average TM–O bond distances and 2NN (second nearest neighbour) interatomic distances from Ni (circles) and Co (triangles) sites in lithiated (filled symbols) and delithiated state (half-filled symbols) for fresh electrodes and electrodes under different ageing conditions (h).

than $\chi(R)^{Co}$, indicating contrasting local structural effects around Ni and Co. Delithiation causes an overall increase of the $\chi(R)$ amplitude, which is much more pronounced for $\chi(R)^{Ni}$ in comparison to $\chi(R)^{Co}$. This points to an increased structural order in the local environment around Ni as compared to Co upon delithiation, as also indicated by feature C in Fig. 3. This difference is most noticeable for the O-environment (peak D) and much lower in the higher shell environment (peak E). The effects of structural relaxation caused by charge compensation are highly localized, occurring under a clearly established long-range hexagonal symmetry.

Fig. 5h shows the bond distances for Ni–O (R_{Ni-O}) and Co–O (R_{Co-O}) atom pairs for all the samples extracted from $\chi(R)$, where the circles and triangles represent Ni–O and Co–O pairs respectively, while closed symbols and half-filled symbols represent lithiated and delithiated states. It is clear that under lithiated conditions, Ni–O bonds are typically longer than Co–O bonds while the bond distances are similar in the delithiated state. In other words, Ni–O_6 assumes a larger octahedral volume than Co–O_6 in the lithiated state and both contract to the same size upon delithiation. Both fresh and aged electrodes reveal that the R_{Ni-O} contraction (~0.06 Å) is almost twice as strong as the R_{Co-O} (~0.03 Å) upon delithiation of the material (from SoC 0% to SoC 100%). This stronger contraction of Ni–O bonds is most likely a direct consequence of a stronger oxidation of Ni compared to Co. A greater change in the TM–O bond is generally seen for the aged electrodes. It is noted that the structural long-range order changes which are typically observed using *operando* X-ray diffraction in NCA material[13] thus appears to be dominated by changes in Ni–O_6 rather than Co–O_6 octahedron size (ESI Fig. S5†).

The average TM–TM interatomic distances (R_{TM-TM}) extracted from fits (second peak E) to the Ni and Co K-edges are plotted in Fig. 5h. We find that for both Ni and Co, R_{TM-TM} becomes systematically shorter in the delithiated state for all three different electrodes. A closer inspection reveals that the average R_{TM-TM} value decreased by ~0.05 Å for a Ni site and ~0.03 Å for a Co site respectively. These values are close to R_{Ni-O} and R_{Co-O} bond contraction values when the material is delithiated. The structural changes in the higher shells (TM–TM) upon delithiation are hence relatively smaller as compared to the O-environment. This is also evident when we compare all three electrodes under lithiated conditions, where we find $R_{Ni-TM} \sim R_{Co-TM}$, but $R_{Ni-O} > R_{Co-O}$ for any given electrode. This indicates that despite strong changes in the local TM environments, the crystallographic structure does not undergo significant phase transformations upon ageing, which is also shown in our previous study.[12] Although the crystallographic structures are very similar, the local structure of the metals exhibits strong dynamics during the redox processes, which is indicative of the activity of the oxygen.

2.4 Direct probe of oxygen redox activity and its change on ageing

As indicated by the results reported above, it is evident that not only the metal but also oxygen plays a significant role in the redox dynamics. The investigation reported below explores the role of oxygen in greater detail, specifically delving into two interconnected processes: formation of the diatomic oxygen contained in the NCA bulk as it is typically observed in Li-rich materials[35] and charge compensation through changes in the hybridized TM–O bonds as demonstrated on NMC materials.[18] The reversible formation of diatomic oxygen has previously been observed for Li-rich materials as well as in other battery chemistries.[27,36,37] The focus of the given study is particularly on non-aqueous Ni-rich transition metal oxide Li-ion cathode materials. Specifically, NCA cathodes (or similar non-Li-rich cathodes) only demonstrated O_2 formation with RIXS at potentials far outside the standard operating potential range (above 4.75 V *vs.* Li/Li^+).[19] As will be shown below from RIXS data, these highly engineered NCA cathodes show reversible diatomic oxygen formation already at potentials lower than 3.8 V.

The investigation starts by examining oxygen charge compensation through changes in hybridization. The O-K-edge TFY X-ray absorption spectra, which reflect the O 2p-character of the unoccupied bands, are presented in Fig. 6 and reveal an increase of the pre-edge area during delithiation for both the fresh and aged samples. The increase in the area of the O K pre-edge is usually ascribed to removal of electrons from neighbouring metal d-orbitals hybridizing with O 2p orbitals.[19,38,39] The increase in the number of unoccupied states is not surprising considering that not only Li ions but also electrons are extracted from the cathode during delithiation. The most drastic change of the oxygen pre-edge occurs when charging between 0 and 50% SoC, supporting that charge compensation from Ni–O_6 rather than the Co–O_6 environment occurs when held at lower potentials.[5] The Fresh and Aged electrodes show very similar O K-edge features at 0% SoC, while at 100% SoC the number of unoccupied states increases in order from Fresh, to Aged H, to Aged L. The results thus show that during

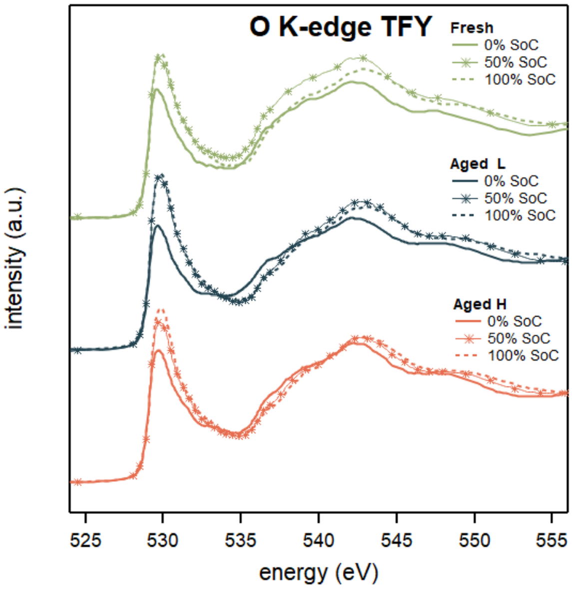

Fig. 6 O K-edge XAS spectra taken in TFY mode of Fresh, Aged L, and Aged H samples in 0, 50 and 100% SoC.

delithiation of the aged material, more electrons from the TM–O hybridized states can be removed (per number of oxygen), compared to the fresh material. This increase of such a charge compensation mechanism is likely linked to the establishment of a higher degree of hybridization for the Ni in aged electrodes, as seen from the Ni K- and L-edges. Complementary PFY O K-edge XAS spectra shown in ESI Fig. S9† support the conclusions drawn from the TFY spectra.

It is noteworthy that the O K-edge TFY of the Aged L and H samples are similar when comparing samples of the same potential against each other, which is demonstrated in Fig. 6. Furthermore, the Fresh 0% SoC sample is also close to identical to both aged samples at 0% SoC with minor increase in intensity on the entire low energy side of the main-edge for the Aged H sample. The Aged L sample in the same low energy region of the main-edge displays a less drastic increase in intensity compared to the Fresh sample. This suggests that ageing in the low SoC region decreases the oxygen activity.

The oxygen chemistry discussed above is complemented by reversible O_2 formation, which is a second process where oxygen participates in the redox reactions. For the material investigated here it is discovered to be produced upon delithiation already below 50% SoC, with greater amounts produced in the 50–100% SoC range. The O K-edge RIXS maps of the Fresh 0% and 100% SoC samples in Fig. 7a and c, respectively, demonstrate the emergence of vibrational signatures as a result of delithiating the NCA, highlighted by a red square and presented in an enhanced view in Fig. 7b and d. These vibrational progressions have a ΔE of approximately 0.19 eV, which corresponds to the stretching mode of O_2 molecules.[40,41] Integrated spectra over the range of 531.2–533.2 eV excitation energies around the vibrational features for all samples can be seen in Fig. 8 where all 100% SoC samples display clear signs of O_2 vibrations. Furthermore, it can be deduced that most of the O_2 produced during charging is reversibly reduced back during discharge since the vibrations of the 0% SoC aged samples show a drastic decrease in the vibrational features.

The vibrational features for the aged 100% SoC samples displayed in Fig. 8 are very similar in intensity while the Fresh

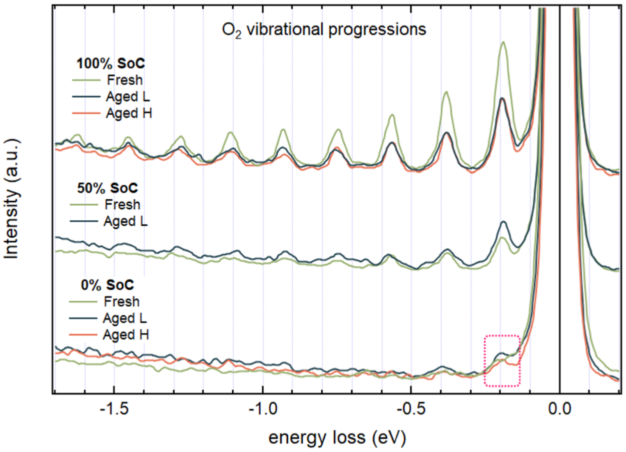

Fig. 8 O K-edge RIXS spectra displaying the region of O_2 vibrations. The spectra are integrated over the excitation energies 531.2–533.2 eV. The red box highlights the difference between Fresh, Aged L, and Aged H samples at 0% SoC.

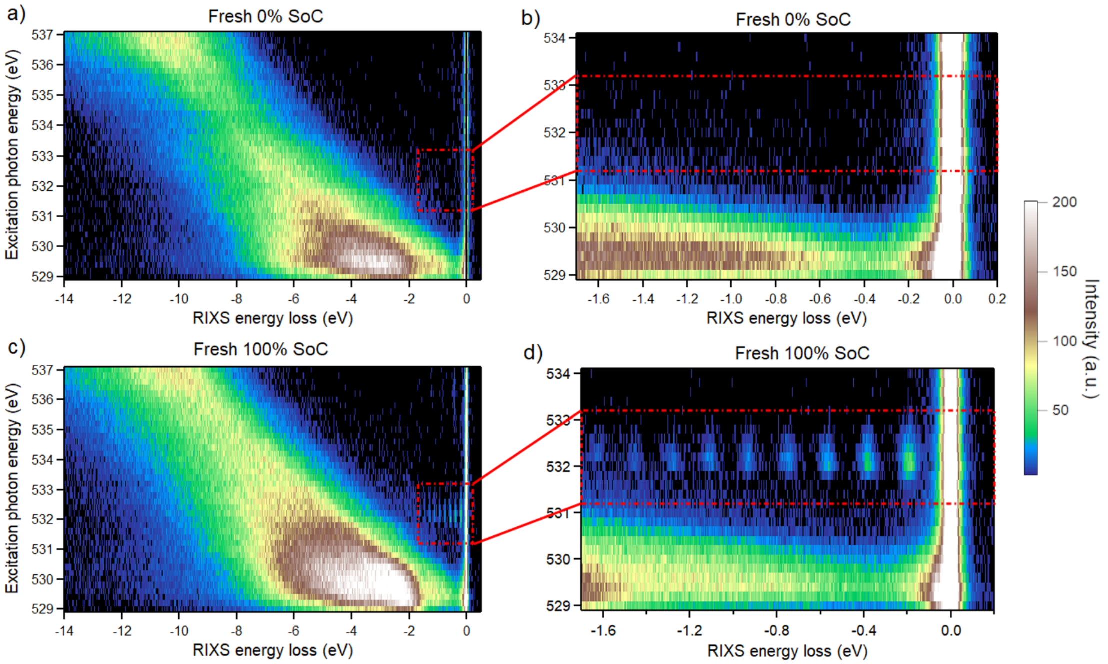

Fig. 7 O K-edge RIXS maps of the Fresh sample in 0% SoC, once showing the whole RIXS map (a) and once focused on the area where vibrational progressions of molecular oxygen are expected (b). The same is repeated for the whole RIXS map of the Fresh 100% SoC sample (c) and the vibrational progression (d).

100% SoC sample display higher intensity for the vibrations. Analysis of the integrated area of the features by multi-peak fitting reveals an intensity drop between the Fresh and the Aged L samples to 47% and between Fresh and Aged H samples to 41% (the details of the fitting and calculation are available in the ESI "RIXS"†). This drop in intensity is proportional to the decrease in reversible oxygen redox during the ageing process and is partly responsible for the decrease in capacity.

By combining the XAS data from both the Ni L-edge and the O K-edge for the Fresh sample, it is seen that Ni participation in the charge compensation is rather constant over the whole SoC range, while oxygen participation through hybridization is involved mainly below 50% SoC. For the Aged samples, both Ni and O participation is more dominant between 0 and 50% SoC than beyond 50% SoC. However, in contrast to fresh samples, for aged electrodes oxygen participation through hybridization starts to occur also in the high SoC region (50–100% SoC). This is seen in the integrated and normalized intensities from the respective RIXS maps see in Fig. S7 with the details on the data treatment in the ESI "RIXS" section.†

From the data presented in Fig. 8, it is estimated that 4.5% of the bulk oxygen is involved in O_2 formation and at least an additional 7.5% of the bulk oxygen takes part in reversible redox reactions. This was estimated by comparison of changes in the spectral weight between samples. The detailed calculations are specified in the ESI "RIXS" section.† Although these numbers provide ballpark figures, it is crucial to acknowledge that these calculations should be treated as rough estimates regarding the amount of O_2 formed or oxygen redox since oxygen diffusion out of the bulk and consumption in secondary reactions, *e.g.* with the electrolyte, are still possible.

Fig. 9 demonstrates the different involvement of O and Ni in charge compensation (a and b correspondingly). Here we evaluate Ni redox participation (comparison of normalized L2/L3 peak ratios) and O participation through bond hybridization (normalized areas of the pre-edge are evaluated for various samples). The left panel of the figure displays the evolution of oxygen hybridization for Fresh, Aged L and Aged H samples. All samples exhibit a similar pattern in the change of the oxygen electronic structure below 50% SoC. Beyond 50% SoC, the Fresh sample shows no evidence of additional oxygen involvement, unlike the Aged samples. In the right panel, Ni redox participation is shown. Interestingly, for Ni, the change of the oxidation state is consistent throughout the whole SoC range in the Fresh samples. However, in the aged samples, this change intensifies below 50% SoC and diminishes thereafter. These observed trends could suggest an increasing significance of the oxygen involvement as the material degrades.

2.5 Aluminum as a redox inactive metal

Although aluminum is present in the NCA structure and acts to enhance material stability, it has been observed that Al does not participate significantly in the redox chemistry.[42] This statement was confirmed also for these electrodes by means of hard X-ray photoelectron spectroscopy (HAXPES) as shown in the ESI "HAXPES" section.† The Al 1s spectra were recorded for both fresh and aged electrodes in lithiated and delithiated states. The spectra show no significant variation between all samples; therefore, the participation of Al in the charge compensation was interpreted as limited.

3 Discussion

In the simplified description of LIB redox reactions, $LiTMO_2 \rightleftharpoons TMO_2 + Li^+ + e^-$, the redox active elements are generally referred to the metals, *i.e.* Ni and Co. However, according to the recent understanding, redox reactions are described in processes involving both TM and O, where the cationic redox occurs within the cathode material stability region and oxygen participation accounts for the capacity delivered beyond that.[19,43–46] The results presented above clearly demonstrated an expanded

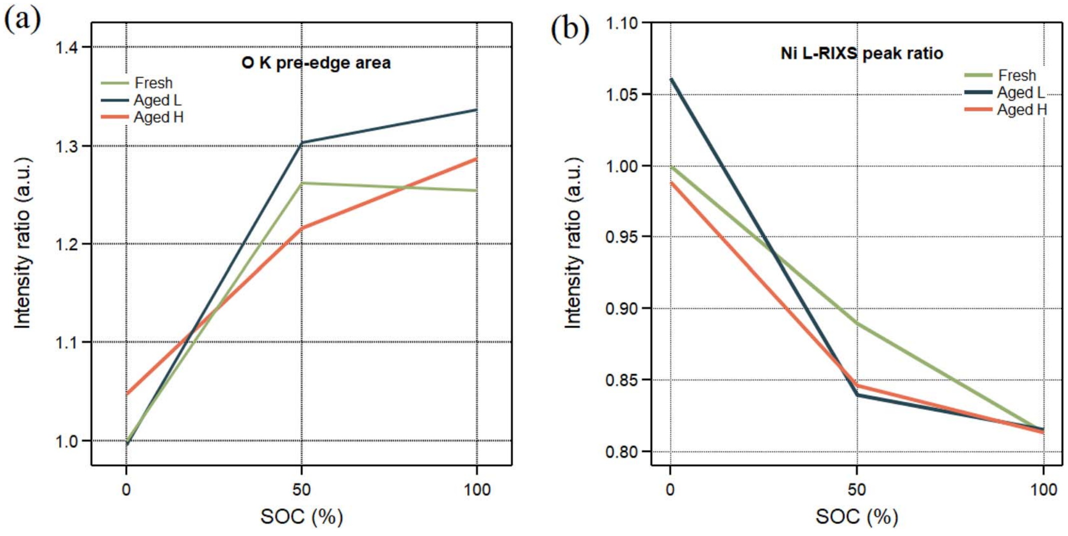

Fig. 9 The integrated pre-edge area of the O K-edge XAS spectra is compared (a). The ratios of integrated areas from the Ni L-edge RIXS data are shown (b).

perspective to comprehend the redox activity in these transition metal oxide materials upon ageing, particularly including the role of oxygen. It is evident that the different charge compensation mechanisms need to be considered throughout the whole lithiation/delithiation cycle. LAM is a pertinent part of positive electrode degradation.[12,47] One can summarize LAM mechanisms as a loss of accessible redox centres and/or availability to host Li ions in the material. A previous study conducted on an extended ageing matrix[12] has demonstrated that the commonly assumed issues of particle cracking and formation of secondary phases have been largely addressed reaching a level suitable for battery applications in highly engineered electrodes. In light of the present article, it is clear that to progress further in developing long-term stable batteries addressing of the redox activity is needed also while determining mechanisms in ageing of batteries.

The starting point of the current investigation is the evaluation of Ni and Co redox activity and its deterioration upon material ageing. During the delithiation of the fresh NCA electrode, Ni is shown to be the primary element participating in electron compensation, while cobalt contained in the NCA has shown significantly lower redox activity (Fig. 3). Despite an expected discrepancy in Ni participation in charge compensation between Fresh and Aged samples, the study has shown that while not all the Ni oxidizes at higher states of charge, the relative amount does not change after ageing (Fig. 4). This might indirectly indicate that the often assumed mechanism of LAM due to phase transformation or isolation with subsequent loss redox available TM[4] is not dominating in the studied case. This also agrees with our previous X-ray diffraction measurements of the NCA samples.[12] The Fresh samples have shown very similar Ni participation in charge compensation in the redox processes occurring throughout 0 to 100% SoC. However, after ageing, the nature of the charge compensation changes and substantial part of Ni charge compensation activity in Aged samples is observed before 50% SoC for both Aged L and Aged H (Fig. 4), which agrees with the study of NCA material by W. Lebens-Higgins *et al.*[19] This is here correlated to a large participation of oxygen also in the 0 to 50% SoC region, where the oxygen activity is mainly linked to changes in the Ni–O hybridization, as well as electron extraction from the hybridized Ni(3d)–O(2p) states.

When comparing the local structure changes around Ni and Co in TM–O_6 octahedra, the role of TM in the charge compensation mechanism was found to be significantly different. In the case of Ni–O_6, the Ni shows a substantial change of the oxidation state with a little contribution from hybridization variations upon delithiation. In the case of Co, the change of the Co oxidation state itself is found to be relatively small, but instead, the hybridization change is found to be rather significant. This highlights the important role of oxygen in the charge compensation mechanism from Co–O_6 and why it requires to be thoroughly investigated. In the context of this article, it is noted that a higher Co content is linked to higher material stability.[48] Co (compared to Ni) is here found to exhibit charge compensation though larger changes in TM–O hybridization, lower degree of TM oxidation state change, and lower change in TM–O bond lengths. This indicates that when charge compensation occurs predominantly through larger changes in TM–O hybridization, the change of the TM oxidation state is lower, in turn leading to smaller TM–O bond relaxations. These findings might be a key for increasing the stability of NCA materials further.

The oxygen participation manifests in two ways observed with spectroscopic techniques: firstly, oxygen participation through hybridization, as discussed above, and secondly formation of diatomic oxygen in classical oxygen redox understanding. Diatomic oxygen formation was found to be more prevalent above 50% SoC (3.8 V *vs.* Li/Li^+) and still significant already below 50% SoC for both Fresh and Aged samples. For the 0% SoC fresh electrode, the amount of O_2 is below the detection limit, while starting from 50% SoC the presence of molecular O_2 can be clearly observed for all samples. This observation contrasts studies that show diatomic oxygen formation only above 4.75 V.[19] Our findings indicate that the formation of molecular O_2 in the NCA material occurs much before the expected threshold of 75% material delithiation. Considering the long lifetime of these NCA batteries, the decrease on lithiation clearly shows reversible oxygen redox, which was seen before for Li-rich materials[35] and Na-ion materials.[49] The estimated amount of O_2 redox is roughly 5% of the total amount of oxygen (calculation details can be found in the ESI section "RIXS"†). From this, it is evident that only a small percentage of the available oxygen actively participates in the reversible formation of molecular oxygen. Still, less O_2 formation is seen in the aged material. Since practical battery life is often limited to over 80% capacity retention, loss of cyclable O_2 needs to be one of the factors to consider in LAM.

The oxygen detected in a diatomic form is trapped in the NCA bulk. The TEM study presented in this paper of Aged H electrodes showed development of nanoporosity within the bulk of the primary particles. The formation of pores in the primary particles upon ageing within the bulk of the NCA active material has not been reported before. However, the formation of similar cavities was observed in LNMO[50] and in the rock-salt surface phase for NCA.[51] However the latter was studied by simulating electrochemical changes using the heating of the material. However, the study[51] suggests that the bulk of the material will not suffer from significant oxygen loss due to the slow oxygen diffusion which contrasts our findings. Yet in agreement with our study, slow oxygen diffusion and the lack of driving force can explain clustering of the vacancies and void formation, probably also facilitated by the changing TM–O_6 volume during cycling. DFT studies have shown that for Li-rich materials oxygen release can initiate the formation of voids in the structure and further clustering.[28] Based on this, we suspect that the observed voids are related to oxygen release. After the formation of oxygen, part of it can be trapped in the bulk; however cumulative increase in O_2 was not observed for this material although some residual amounts of oxygen were detected in Aged H 0 and Aged L 0 samples. In the current study, the results indicate that the dominating part of the O_2 is oxidized and included back into the NCA structure. Still, oxygen redox-driven void formation is supported by other findings,[50] where a previous study proposes that cavities created near the

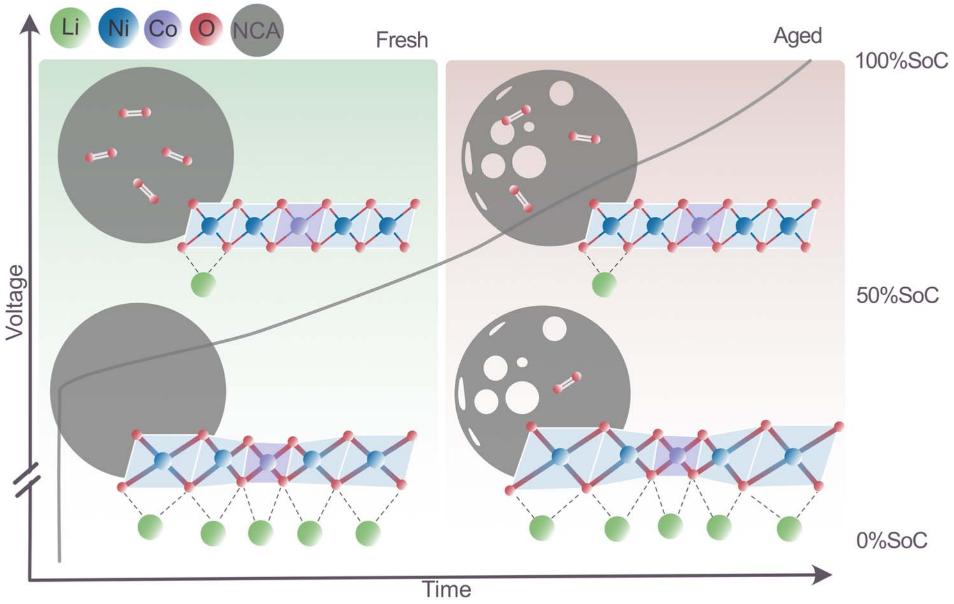

Fig. 10 Schematic overview of the changes observed in the study during cycling of the fresh and aged NCA electrodes. The summary of the charge compensation processes illustrates modifications in the Ni–O_6 and Co–O_6 configurations, as well as the various roles of oxygen participation through hybridization (shown by TM–O) and the formation of diatomic oxygen (shown on particles). Upon the delithiation of the material, there is a noticeable reduction in the size of the octahedra, with more significant alterations observed in the Ni–O_6 environment. Oxygen plays a role *via* hybridization, leading to a shift in TM–O bonds towards a more ionic character. This alteration impacts the Co configuration to a greater degree than the Ni. The formation of diatomic oxygen can be observed even below 3.8 V, with an increasing trend as delithiation progresses towards 100% State of Charge (SoC). After ageing, firstly, the material shows the emergence of nanovoids. Secondly, in the lithiated state, the Ni–O_6 octahedra demonstrate an increase in size and a minor quantity of diatomic oxygen is detected. Thirdly, during delithiation, increased formation of diatomic oxygen occurs below 50% SoC, but beyond 50% SoC, the quantity of diatomic oxygen is less than that observed in the fresh material.

surface migrate towards the bulk. The formed voids can serve as a stress mitigation feature which can explain the significantly lower extent of particle cracking observed for this material. In this context, we recall that the change in local Ni and Co structures associated with cycling is seen primarily in the Ni–O_6 octahedron with change of the Ni–O bond length being twice that of the Co–O bond. This indicates greater Ni–O_6 octahedron contribution to the change of the *c* lattice parameter (most sensitive parameter in this type of material towards delithiation) and, therefore, possibly stress is induced in the material upon cycling (Fig. 5). Upon ageing, the Ni–O bonds become longer and result in even more significant bond contraction and expansion upon cycling.

In terms of ageing, it can be discussed how important these local structural changes and connected stresses are for the NCA material. No significant particle cracking was observed for the aged NCA electrode, implying low impact of stresses on a larger scale. Still it could be argued that lithium diffusion can be influenced by the change in the interlayer distance and subsequent stresses. The increased Ni–O_6 volume on lithiation may alter the lithium diffusion through the material, where a larger/smaller volume may be more/less beneficial for the lithium diffusion. In this context the redox activity with more charge compensation from Co–O hybridization and less Co–O_6 volume changes thus would provide a more stable material. In addition, the voids in the material will result in higher tortuosity and an increase of Li-ion diffusion resistance, a phenomenon which is also observed for these samples in our previous study.[12] In the current study, we did not aim to correlate it; however, it is important to investigate this phenomenon in the future.

4 Conclusions

The present study of automotive-grade $LiNi_xCo_yAl_zO_2$ (NCA) positive Li-ion battery electrodes investigates the redox mechanisms in fresh and aged cells (>900 cycles and capacity retention 75%). A particular focus is placed on the role of oxygen, and the results offer important new insights to be utilized in the design of next-generation high-stability Li-ion batteries. The structural and electronic differences seen in Ni, Co and O upon cycling of fresh and aged cells are obtained from a combination of in-house and advanced characterization techniques (TEM, XAS, EXAFS, and RIXS), and the combined results show that an expanded perspective is necessary to comprehend the NCA redox mechanisms and their change on ageing.

The key findings of the study are summarized in Fig. 10. The role of oxygen in the charge compensation is found to be twofold: in fresh electrodes, oxygen participates through changes in bond hybridization, a mechanism that is dominant below 50% SoC, and through oxygen redox with diatomic molecule formation, a mechanism found mostly above 50% SoC but much before the expected threshold of 75% material delithiation (*i.e.* below 3.8 V). Both oxygen redox mechanisms are reversible in fresh and aged NCA materials; however, upon ageing, residual molecular oxygen was found in 0% SoC aged samples. At the same state, the material develops a large number of nanopores (dominantly in the range of 4–12 nm in size), which might be associated with the process of O_2 formation. In the lithiated state, one can describe the TM–O layer in fresh NCA in terms of a long-range ordered hexagonal arrangement of larger Ni–O_6 with higher disorder ($\sigma_{\text{Ni–O}}{}^2$) and smaller Co–O_6 octahedra with lower disorder ($\sigma_{\text{Co–O}}{}^2$). As Li is removed from the fresh NCA material, there is a stronger oxidation of Ni and a stronger volume contraction in the local environment around Ni sites, in contrast to Co. During delithiation, the change in Ni–O bonds is substantial, being reduced to a similar size to the Co–O bond length. In the aged NCA material, the size of the TM–O octahedra in the delithiated state is unchanged, while it is seen to increase for Ni–O_6 in the lithiated state. The TM–O hybridization is stronger in the Co–O_6 environment compared to the Ni–O_6 environment, and the combined results indicate that this may be key for the long-term stability of the layered TM oxide structure. Co, known to provide a more stable TM–O structure than Ni, utilizes changes in the hybridized TM–O bonds as a charge compensation mechanism, which result in a smaller change in the TM oxidation state and fewer structural changes associated with the TM–O_6 on cycling.

Finally, by investigating state-of-the-art commercial batteries this study aims to narrow the gap between industry and academic research. The study provides fundamental new insights into the mechanism of the loss of active material in automotive-grade LIBs, offering the possibility to accelerate the development of future long-term stable cathode materials.

Author contributions

Anastasiia Mikheenkova: conceptualization, data curation, formal analysis, investigation, methodology, project administration, resources, software, validation, visualization, writing – original draft, and writing – review & editing. Soham Mukherjee: conceptualization, data curation, formal analysis, investigation, methodology, software, validation, visualization, writing – original draft, and writing – review & editing. Moritz Hirsbrunner: conceptualization, data curation, formal analysis, investigation, methodology, software, validation, visualization, writing – original draft, and writing – review & editing. Pontus Törnblom: data curation, formal analysis, methodology, investigation, software, validation, writing – original draft, and writing – review & editing. Cheuk-Wai Tai: conceptualization, data curation, formal analysis, funding acquisition, investigation, methodology, resources, software, validation, and writing – review & editing. Carlo U. Segre: investigation, methodology, software, and writing – review & editing. Yujia Ding: investigation, methodology, and software. Wenliang Zhang: investigation, methodology, and software. Teguh Citra Asmara: investigation, methodology, and software. Yuan Wei: investigation, methodology, and software. Thorsten Schmitt: investigation, methodology, and software. Håkan Rensmo: funding acquisition, supervision, and writing – review & editing. Laurent Duda: conceptualization, data curation, formal analysis, funding acquisition, investigation, methodology, software, supervision, validation, visualization, writing – original draft, and writing – review & editing. Maria Hahlin: conceptualization, funding acquisition, methodology, project administration, supervision, resources, data curation, writing – original draft, and writing – review & editing.

Conflicts of interest

There are no conflicts to declare.

Acknowledgements

The authors acknowledge Bertrand Philippe for providing the cells for the current study, Niladri Roy Chowdhury together with Torbjörn Thiringer for providing aged cells, Matthew J. Lacey for opening fresh cells and Alexander J. Smith for opening the aged cells. The authors acknowledge the P. Bruce Oxford group (Robert A. House) for the preparation of the Li-rich NMC material. The authors also acknowledge Olivier Donzel-Gargand for FIB preparation of the samples. Parts of this research was carried out at PETRA III and we would like to thank Akhil Tayal for assistance in using P64. We acknowledge DESY (Hamburg, Germany), a member of the Helmholtz Association HGF, for the provision of experimental facilities. Beamtime was allocated for proposal I-20211450. Additionally, the authors acknowledge the financial support from the Swedish Energy Agency to the projects “Ageing of Lithium-ion Batteries with Nickel-Rich Cathodes for Electromobility” (project number: 45538-1) and “X-ray based methodology for next generation Na-ion battery cathodes” (project number: 50745-1), as well as StandUP for Energy Consortium, Sweden. The soft X-ray XAS and RIXS experiments were performed at the ADRESS beamline of the Swiss Light Source at the Paul Scherrer Institut (PSI). The experimental work at PSI is supported by the Swiss National Science Foundation through project nos. 178867 and 207904. T. C. A. and Y. W. acknowledge funding from the European Union's Horizon 2020 research and innovation programme under the Marie Sklodowska-Curie grant agreement No. 701647 and 884104 (PSI-FELLOW-II-3i program). Cheuk-Wai Tai acknowledges the support from the Swedish Research Council (2018-05260). Moritz Hirsbrunner, Pontus Törnblom, Håkan Rensmo, Laurent Duda, and Maria Hahlin acknowledge the Swedish Research Council (project number: 2018-06465 and 2022-06076). This work was performed, in part, at the Electron Microscopy Centre, supported by the Department of Materials and Environmental Chemistry and Faculty of Science at Stockholm University, Sweden. MRCAT operations are supported by the Department of Energy and the MRCAT member institutions. This research used resources of the Advanced Photon Source, a U.S. Department of Energy (DOE) Office of Science User Facility operated for the DOE Office of Science by Argonne National Laboratory under Contract No. DE-AC02-06CH11357. We acknowledge Myfab Uppsala for providing facilities and experimental support. Myfab is funded by the Swedish Research Council (2019-00207) as a national research infrastructure.

Notes and references

1 S. Pauliuk, N. Heeren, P. Berrill, T. Fishman, A. Nistad, Q. Tu, P. Wolfram and E. G. Hertwich, *Nat. Commun.*, 2021, **12**, 5097.

2 J. T. Frith, M. J. Lacey and U. Ulissi, *Nat. Commun.*, 2023, **14**, 420.

3 J. U. Choi, N. Voronina, Y.-K. Sun and S.-T. Myung, *Adv. Energy Mater.*, 2020, **10**, 2002027.

4 J. S. Edge, S. O'Kane, R. Prosser, N. D. Kirkaldy, A. N. Patel, A. Hales, A. Ghosh, W. Ai, J. Chen, J. Yang, S. Li, M.-C. Pang, L. B. Diaz, A. Tomaszewska, M. Waseem Marzook, K. N. Radhakrishnan, H. Wang, Y. Patel, B. Wu and G. J. Offer, *Phys. Chem. Chem. Phys.*, 2021, **23**, 8200–8221.

5 A. Manthiram, *Nat. Commun.*, 2020, **11**, 1550.

6 J. Kasnatscheew, S. Röser, M. Börner and M. Winter, *ACS Appl. Energy Mater.*, 2019, **2**, 7733–7737.

7 H. Darjazi, E. Gonzalo, B. Acebedo, R. Cid, M. Zarrabeitia, F. Bonilla, M. Ã. Munoz-Marquez and F. Nobili, *Mater. Today Sustain.*, 2022, **20**, 100236.

8 J. Wu, H. Zhu, H. Yu, Z. Wang, H. Jiang and C. Li, *Ind. Eng. Chem. Res.*, 2022, **61**, 2817–2824.

9 K.-J. Park, M.-J. Choi, F. Maglia, S.-J. Kim, K.-H. Kim, C. S. Yoon and Y.-K. Sun, *Adv. Energy Mater.*, 2018, **8**, 1703612.

10 G. Qian, J. Wang, H. Li, Z.-F. Ma, P. Pianetta, L. Li, X. Yu and Y. Liu, *Natl. Sci. Rev.*, 2022, **9**, nwab146.

11 C. Liao, F. Li and J. Liu, *Nanomaterials*, 2022, **12**, 1888.

12 A. Mikheenkova, A. J. Smith, K. B. Frenander, Y. Tesfamhret, N. R. Chowdhury, C.-W. Tai, T. Thiringer, R. W. Lindström, M. Hahlin and M. J. Lacey, *J. Electrochem. Soc.*, 2023, **170**, 080503.

13 A. Mikheenkova, O. Gustafsson, C. Misiewicz, W. R. Brant, M. Hahlin and M. J. Lacey, *J. Energy Storage*, 2023, **57**, 106211.

14 S. S. Zhang, *Energy Storage Mater.*, 2020, **24**, 247–254.

15 B. Rowden and N. Garcia-Araez, *Energy Rep.*, 2020, **6**, 10–18.

16 R. Jung, M. Metzger, F. Maglia, C. Stinner and H. A. Gasteiger, *J. Electrochem. Soc.*, 2017, **164**, A1361.

17 T. Hatsukade, A. Schiele, P. Hartmann, T. Brezesinski and J. Janek, *ACS Appl. Mater. Interfaces*, 2018, **10**, 38892–38899.

18 K. Kleiner, C. A. Murray, C. Grosu, B. Ying, M. Winter, P. Nagel, S. Schuppler and M. Merz, *J. Electrochem. Soc.*, 2021, **168**, 120533.

19 Z. W. Lebens-Higgins, N. V. Faenza, M. D. Radin, H. Liu, S. Sallis, J. Rana, J. Vinckeviciute, P. J. Reeves, M. J. Zuba, F. Badway, N. Pereira, K. W. Chapman, T.-L. Lee, T. Wu, C. P. Grey, B. C. Melot, A. V. D. Ven, G. G. Amatucci, W. Yang and L. F. J. Piper, *Mater. Horiz.*, 2019, **6**, 2112–2123.

20 N. Ikeda, I. Konuma, H. B. Rajendra, T. Aida and N. Yabuuchi, *J. Mater. Chem. A*, 2021, **9**, 15963–15967.

21 A. Menon, B. Johnston, S. Booth, L. Zhang, K. Kress, B. Murdock, G. Paez Fajardo, N. Anthonisamy, N. Tapia-Ruiz, S. Agrestini, M. Garcia-Fernandez, K. Zhou, P. Thakur, T. Lee, A. Nedoma, S. Cussen and L. Piper, *PRX Energy*, 2023, **2**, 013005.

22 A. O. Kondrakov, H. Geßwein, K. Galdina, L. de Biasi, V. Meded, E. O. Filatova, G. Schumacher, W. Wenzel, P. Hartmann, T. Brezesinski and J. Janek, *J. Phys. Chem. C*, 2017, **121**, 24381–24388.

23 S. Sharifi-Asl, J. Lu, K. Amine and R. Shahbazian-Yassar, *Adv. Energy Mater.*, 2019, **9**, 1900551.

24 T. Li, X.-Z. Yuan, L. Zhang, D. Song, K. Shi and C. Bock, *Electrochem. Energy Rev.*, 2020, **3**, 43–80.

25 W. M. Dose, I. Temprano, J. P. Allen, E. Björklund, C. A. O'Keefe, W. Li, B. L. Mehdi, R. S. Weatherup, M. F. L. De Volder and C. P. Grey, *ACS Appl. Mater. Interfaces*, 2022, **14**, 13206–13222.

26 S. E. Renfrew and B. D. McCloskey, *ACS Appl. Energy Mater.*, 2019, **2**, 3762–3772.

27 L. C. Duda and K. Edström, *J. Electron Spectrosc. Relat. Phenom.*, 2017, **221**, 79–87.

28 R. A. House, G. J. Rees, M. A. Pérez-Osorio, J.-J. Marie, E. Boivin, A. W. Robertson, A. Nag, M. Garcia-Fernandez, K.-J. Zhou and P. G. Bruce, *Nat. Energy*, 2020, **5**, 777–785.

29 K. R. Tallman, G. P. Wheeler, C. J. Kern, E. Stavitski, X. Tong, K. J. Takeuchi, A. C. Marschilok, D. C. Bock and E. S. Takeuchi, *J. Phys. Chem. C*, 2021, **125**, 58–73.

30 C. Yang, R. Shao, Q. Wang, T. Zhou, J. Lu, N. Jiang, P. Gao, W. Liu, Y. Yu and H. Zhou, *Energy Storage Mater.*, 2021, **35**, 62–69.

31 A. Anspoks and A. Kuzmin, *J. Non-Cryst. Solids*, 2011, **357**, 2604–2610.

32 C. Gougoussis, M. Calandra, A. Seitsonen, C. Brouder, A. Shukla and F. Mauri, *Phys. Rev. B*, 2009, **79**, 045118.

33 T. Yamamoto, *X-Ray Spectrom.*, 2008, **37**, 572–584.

34 L. Simonelli, E. Paris, C. Iwai, K. Miyoshi, J. Takeuchi, T. Mizokawa and N. L. Saini, *J. Phys.: Condens. Matter*, 2017, **29**, 105702.

35 Q. Li, D. Ning, D. Wong, K. An, Y. Tang, D. Zhou, G. Schuck, Z. Chen, N. Zhang and X. Liu, *Nat. Commun.*, 2022, **13**, 1123.

36 C. Ma, J. Alvarado, J. Xu, R. J. Clément, M. Kodur, W. Tong, C. P. Grey and Y. S. Meng, *J. Am. Chem. Soc.*, 2017, **139**, 4835–4845.

37 M. Li, X. Bi, K. Amine and J. Lu, *Acc. Chem. Res.*, 2020, **53**, 1436–1444.

38 F. M. F. de Groot, M. Grioni, J. C. Fuggle, J. Ghijsen, G. A. Sawatzky and H. Petersen, *Phys. Rev. B*, 1989, **40**, 5715–5723.

39 S. Lafuerza, G. Subías, J. García, S. Di Matteo, J. Blasco, V. Cuartero and C. R. Natoli, *J. Phys.: Condens. Matter*, 2011, **23**, 325601.

40 A. Weber and E. A. McGinnis, *J. Mol. Spectrosc.*, 1960, **4**, 195–200.

41 N. R. Avery, *Chem. Phys. Lett.*, 1983, **96**, 371–373.

42 L. Zou, J. Li, Z. Liu, G. Wang, A. Manthiram and C. Wang, *Nat. Commun.*, 2019, **10**, 3447.

43 K. Luo, M. R. Roberts, R. Hao, N. Guerrini, D. M. Pickup, Y.-S. Liu, K. Edström, J. Guo, A. V. Chadwick, L. C. Duda and P. G. Bruce, *Nat. Chem.*, 2016, **8**, 684–691.

44 K. Luo, M. R. Roberts, N. Guerrini, N. Tapia-Ruiz, R. Hao, F. Massel, D. M. Pickup, S. Ramos, Y.-S. Liu, J. Guo, A. V. Chadwick, L. C. Duda and P. G. Bruce, *J. Am. Chem. Soc.*, 2016, **138**, 11211–11218.

45 M. Li, T. Liu, X. Bi, Z. Chen, K. Amine, C. Zhong and J. Lu, *Chem. Soc. Rev.*, 2020, **49**, 1688–1705.

46 J. Wu, Z. Zhuo, X. Rong, K. Dai, Z. Lebens-Higgins, S. Sallis, F. Pan, L. F. J. Piper, G. Liu, Y.-d. Chuang, Z. Hussain, Q. Li, R. Zeng, Z.-x. Shen and W. Yang, *Sci. Adv.*, 2020, **6**, eaaw3871.

47 H. Sun, B. Jiang, H. You, B. Yang, X. Wang, X. Wei and H. Dai, *Energies*, 2021, **14**, 350.

48 M. Li and J. Lu, *Science*, 2020, **367**, 979–980.

49 W. E. Gent, K. Lim, Y. Liang, Q. Li, T. Barnes, S.-J. Ahn, K. H. Stone, M. McIntire, J. Hong, J. H. Song, Y. Li, A. Mehta, S. Ermon, T. Tyliszczak, D. Kilcoyne, D. Vine, J.-H. Park, S.-K. Doo, M. F. Toney, W. Yang, D. Prendergast and W. C. Chueh, *Nat. Commun.*, 2017, **8**, 2091.

50 P. Yan, J. Zheng, Z.-K. Tang, A. Devaraj, G. Chen, K. Amine, J.-G. Zhang, L.-M. Liu and C. Wang, *Nat. Nanotechnol.*, 2019, **14**, 602–608.

51 H. Zhang, B. M. May, F. Omenya, M. S. Whittingham, J. Cabana and G. Zhou, *Chem. Mater.*, 2019, **31**, 7790–7798.